Electronic Supplementary Information

An Ambient Temperature, CO_2-Assited Solution Processing of Amorphous Cobalt Sulfide in Thiol/Amine Based Quasi-Ionic Liquid for Oxygen Evolution Catalysis

Xinhui Zhao,[a] Jingyun Jiang,[a] Zhimin Xue,[b] Chuanyu Yan[a] and Tiancheng Mu*[a]

[a] Department of Chemistry, Renmin University of China, Beijing 100872, China. Tel: 86-10-6251492, E-mail: tcmu@ruc.edu.cn.

[b] Beijing Key Laboratory of Lignocellulosic Chemistry, College of Materials Science and Technology, Beijing Forestry University, Beijing 100083, China.

Table of the contents

1. Experiment Section

Chemicals

1,2-ethanedithiol ($C_2H_6S_2$, 99.0%, GC) and n-butylamine ($C_4H_{11}N$, 99.0%, GC) were purchased from TCI. Elemental cobalt (Co, 99.98%), iron (Fe, 99.8%), nickel(III) oxide (Ni_2O_3, 99.8%), sulfur (S, 99.99%) and selenium powder (Se, 99.99%) were obtained from Alfa Aesar. Carbon dioxide (CO_2, 99.995%) was bought from Beijing Beiwen Gas factory (Beijing, China). All chemicals were used directly without further purification.

The synthesis of amorphous cobalt sulfide nanosheets

Amorphous cobalt sulfide nanosheets (CoS_x NSs) were synthesized by CO_2-assited solution-processed method. Elemental cobalt (29.5 mg, 0.50 mmol) and sulfur (16.0 mg, 0.50 mmol) were added to a vial followed by 4 mL of n-butylamine and 1 mL of 1,2-ethanedithiol. The solids were dissolved within 60 min under magnetic stirring (1100 rpm), at ambient temperature and pressure (23 ± 2 °C, 1 atm). Neither n-butylamine nor 1,2-ethanedithiol can dissolve elemental cobalt even with slight heating. Optically clear, olive brown ink was obtained upon filtering with a 0.45 μm PTFE (poly-tetrafluoroethylene) filter. The limited concentration of precursor solution is 150 mM in EDT-BA, which is determined by empirical method. Then the solution was quickly transferred to a stainless steel autoclave (volume: ~10 mL) and CO_2 was charged into autoclave to the desired pressure (6 MPa) by DB-80 high-pressure syringe pump (Beijing Spacecrafts Corp., China). After a reaction of 3 h under magnetic stirring (1100 rpm), CO_2 was slowly released. Finally, the precipitates were washed thoroughly with acetone three times and then dried in air at 60 °C for 12 h. The crystalline CoS_x-400 and CoS_x-800 were obtained by annealing amorphous CoS_x in tube furnace at desired temperature for 2 h with a rate of 5 °C min^{-1} in N_2 atmosphere.

Other transition metal chalcogenides were prepared with the same method above.

Characterizations

The XRD patterns of the samples were recorded using an X-ray diffractometer (Rigaku D/Max-2500) using Cu Kα as X-ray radiation (λ = 1.5418 Å) under 40 kV and 30 mA. Data were collected in Bragg-Brettano mode using 0.02° divergence with a scan rate of 2° min^{-1}.

The SEM images, EDX spectra and elemental mapping images of the samples were acquired using a Hitachi SU 8010 field emission scanning electron microscope coupled with energy dispersive X-ray spectroscopy operated at 15.0 kV. The samples were prepared by dropping catalyst powder dispersed in isopropanol onto 300 nm silicon dioxide-coated silicon wafer (Zhejiang Lijing Technology Corp., China) using micropipettes and were dried under ambient conditions. The TEM, HRTEM, STEM-EDX mapping images and SAED patterns were carried out using a JEM-2100F field emission transmission electron microscope coupled with energy dispersive X-ray spectroscopy operated at 200.0 kV. The samples were prepared by dropping catalyst powder dispersed in isopropanol onto carbon-coated copper TEM grids (Beijing Xinxing Braim Technology Corp., China) using micropipettes and were dried under ambient conditions. The Raman spectra were conducted using a FT Bruker RFS 106/S spectrometer equipped with a 532 nm laser. The XPS analyses were performed using a Thermo Scientific ESCA Lab 250Xi at 200 W monochromatic Al Kα radiation. N_2 adsorption-desorption isotherms of the samples were measured at 77 K using Belsorp-Mini II (BEL Japan Inc., Japan). Prior to the measurements, the samples were outgassed under vacuum for 3 h at 100 °C. Thermal gravimetric analysis (TGA) was conducted by the instrument (Q50, TA Instrument Company, America). The conductivities of the EDT-BA quasi-ionic liquid were measured by using a conductivity meter (DDS-11AW, Shanghai Bante Instrument Corp., China).

Mechanism of formation of amorphous CoS_x

The formation of amorphous CoS_x consists of two steps. Firstly, elemental cobalt and sulfur were dissolved and formed Co-S in the DET-BA quasi-ionic liquid. The formation of Co-S was testified by the UV-vis spectrum in Fig. S3. Then, CoS_x NSs were precipitated from EDT-BA by compressed CO_2. Studies had shown the existence of N-H···S hydrogen bonding in thiol-amine mixtures.[1] It is highly possible the CO_2 molecular occupies the bulk volume of the quasi-ionic liquid EDT-BA and cleaves the N-H···S hydrogen bonding between EDT and BA.[2] On the other hand, the EDT^{2-} is actively binding with CO_2 to give a S-bound thiocarbonate through a nucleophilic addition reaction.[3] Thus, compressed CO_2 could strangle the solvency of the quasi-ionic liquid by disturbing the interaction of Co-S/EDT/BA system and then precipitate the dissolved Co-S species gradually.

***In situ* UV-vis**

UV-vis experiments were performed on a UV-3600 Plus UV-Vis-NIR Spectroscopy (Shimadzu Corp., Japan) with a high-pressure view autoclave bought from Beijing Chichenghuaxing Sci & Tech Corp., China. Then the inks were transferred to the high-pressure view autoclave. All data were collected using a medial rate (5 nm s^{-1}) in the spectral range of 300 to 800 nm and triplicates of each sample were measured at ambient temperature.

Electrochemical measurements

The electrocatalytic activity of samples for OER was studied in three-electrode configuration in 1.0 M KOH (pH = 13.8) aqueous electrolyte and recorded on a CHI 660E Electrochemical Workstation (Shanghai Chenhua Instrument Corp., China) at ambient temperature. The glassy carbon electrode (GCE) (diameter: 3 mm, area: 0.07069 cm^2) and Au (111) electrode (diameter: 2 mm, area: 0.0314 cm^2) were first polished with aluminum oxide slurry and thoroughly cleaned with deionized water before use. The nickel foams (NFs) (Shanxi Lizhiyuan Materials Corp., China) was sequentially sonicated in deionized water, ethanol, 3 M HCl solution, and deionized water. The gold-plated nickel foam (gold-NF) was obtained by sputtering NFs with gold for 40 s in a Magnetron Ion Sputter Metal Coating Device (IXRF Systems, Inc., Japan). Besides, electroplating method was also used to cover NF with gold. The electroplating was operated by means of electrochemical deposition from an aqueous solution containing 0.035 mol L^{-1} of $K[Au(CN)_2]$ and 0.73 mol L^{-1} of KH_2PO_4 at 55 °C under constant potential of -0.8 V *vs.* SCE.[4] Saturated calomel electrode (SCE) and platinum wire were used as reference and counter electrodes, respectively. Unless otherwise stated, all experiments were performed at ambient temperature (23 ± 2 °C) and electrode potentials were converted to the RHE scale using E(RHE) = E(SCE) + 0.242 V + 0.059 * pH. Also, all data were collected by using the CHI software and all electrodes above were from CH Instruments, Inc. (Shanghai Chenhua Instrument Corp., China) unless stated else.

We also assemble a two electrode setup in 1.0 M KOH solution with Pt-CoS_x couple catalyst (Fig. S28). A current density of 10 mA cm^{-2} was delivered with a cell voltage of 1.58 V, that is, a combined overpotential of about 350 mV for electrochemical overall water splitting.

Typically, 3 mg of catalyst powder was dispersed in 1 mL mixture of water and ethanol (1:1, v/v) and then 20 mL of Nafion solution (5 wt. % in water and 1-propanol, DuPont D-520) was added. The suspension was immersed in an ultrasonic bath for 30 min to prepare a homogeneous ink. The working electrodes were prepared by depositing 5 μl catalyst ink onto GCE (catalyst loading: ~0.21 mg cm^{-2}), 3 μl catalyst ink onto Au (111) electrode (catalyst loading: ~0.28 mg cm^{-2}) and 20 μl catalyst ink onto gold-NF (0.5*0.5 cm^2, catalyst loading: ~0.24 mg cm^{-2}), respectively.

For temperature-dependent measurements, the sealed electrolytic cell was suspended in a thermostatic oil bath (DF-101S, Henan Yuhua Instrument Factory, China). The cell was held for 10 min at the desired temperature before measured. The effect of temperature on the performance of the catalyst is shown in Fig. S17. As we can see, the OER performance increased with the increase of temperature. The activation energy (E_a) for OER can be determined using the Arrhenius relationship:[5]

$$\frac{\partial(\log j_0)}{\partial(1/T)} = -\frac{E_a}{2.303R}$$

where j_0 is the exchange current density (obtained from Tafel plots), T is the temperature, and R is the universal gas constant. From the slope of the Arrhenius plot (Fig. 4c), the apparent electrochemical activation energy (E_a) can be extracted.

The Faradic efficiency (FE) was calculated from the total charge *Q* (C) passed through the cell and the total amount of oxygen produced n (mol). *Q = it*. The experimental evolved O_2 gas amount was measured by gas chromatography analysis (Ar carrier, molecule sieve 5A column, TCD detector). Assuming that four electrons are needed to produce one O_2 molecule, the Faradaic efficiency can be calculated as follows:

$$\eta = \frac{4F * n}{i * t}$$

where *F* is the Faraday constant (96485 s A mol^{-1}), *n* is the total amount of O_2 molecule (0.345 mol), *i* is the current passed through the cell (7.5*10^{-3} A) and *t* is the time (18000 s).

To calculate the turnover frequency (TOF) of the catalyst, we used the following formula:

$$TOF = \frac{\#\ total\ oxygen\ turnover}{\#\ total\ active\ sites}$$

we assumed all cobalt atoms form the active sites, the cobalt content of the catalyst was calculated from the ICP-AES data, then the total active sites in the electrode (NF, 0.5*0.5 cm^2) could be determined by:

$$\#\ total\ active\ sites = \frac{\omega\% * m_{loading} * S * N_A}{W}$$

in our test, ω% is the cobalt content of the catalyst (62.60 %), $m_{loading}$ is catalyst loading (0.24 mg cm^{-2}), *S* is the geometric area of electrode (0.25 cm^2), *W* is the atom weight of cobalt (58.93 g mol^{-1}) and N_A is Avogadro constant (6.02*10^{23} mol^{-1}).

At an overpotential of 300 mV, the total oxygen turnover was calculated from the current density:[6]

$$\#\ total\ oxygen\ turnover = \frac{j * S * N_A}{4 * F}$$

where *j* is the current density at the given overpotential (53.9 mA cm^{-2}), *S* is the geometric area of electrode (0.25 cm^2), N_A is Avogadro constant (6.02*10^{23} mol^{-1}) and *F* is the Faraday constant (96485 s A mol^{-1}).

2. Supplementary Figures

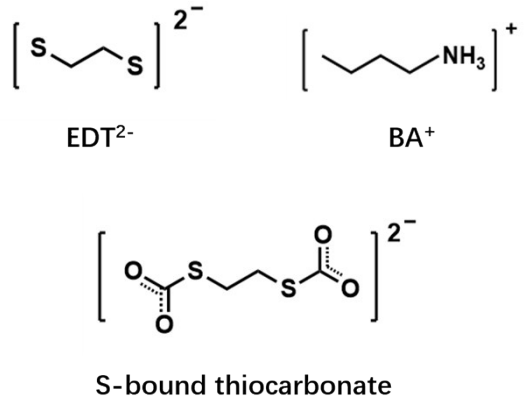

Fig. S1. a) Proposed chemical structures of charged species in this paper; b) Absorption spectra of the solution of Co-S under compressed CO_2.

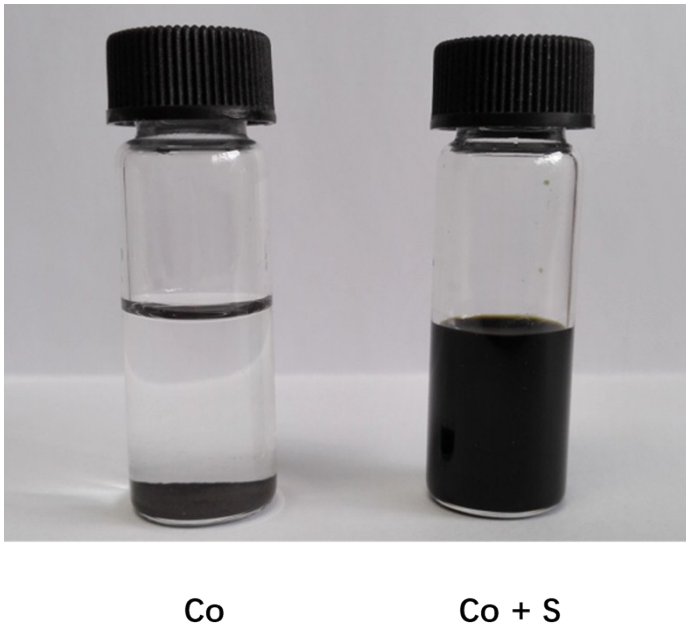

Fig. S2. Photographs of cobalt (left) and cobalt with sulfur (right) powders in EDT-BA solvent.

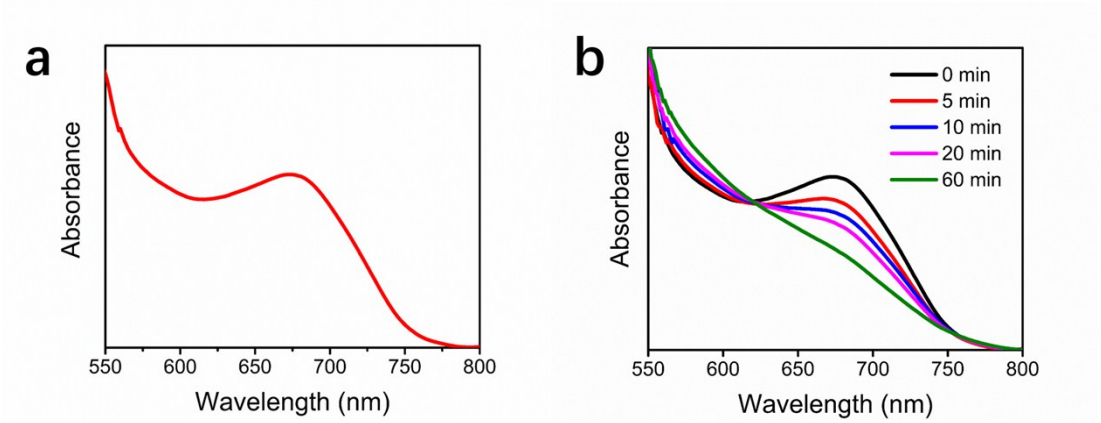

Fig. S3. Absorption spectra of the solution of Co-S a) before and b) after treating with compressed CO_2.

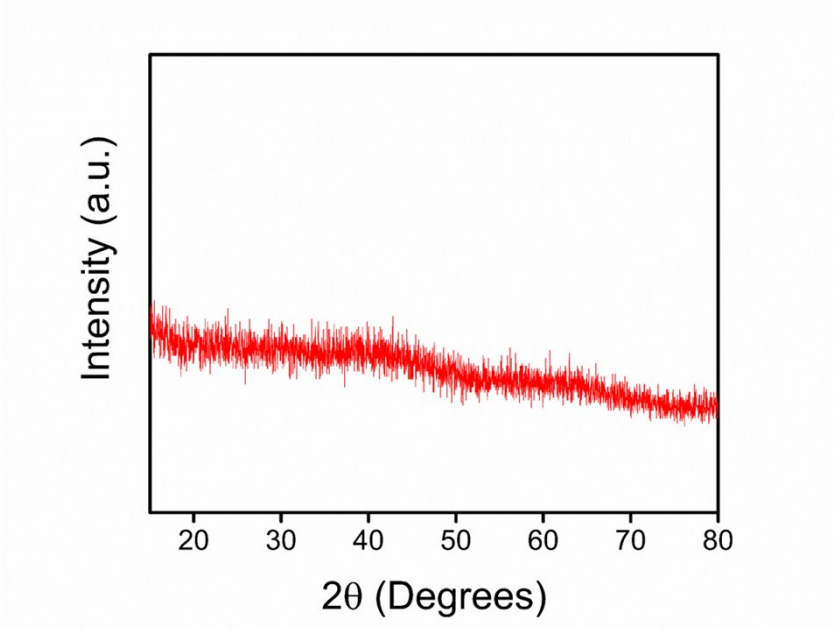

Fig. S4. XRD pattern of the CoS_x NSs.

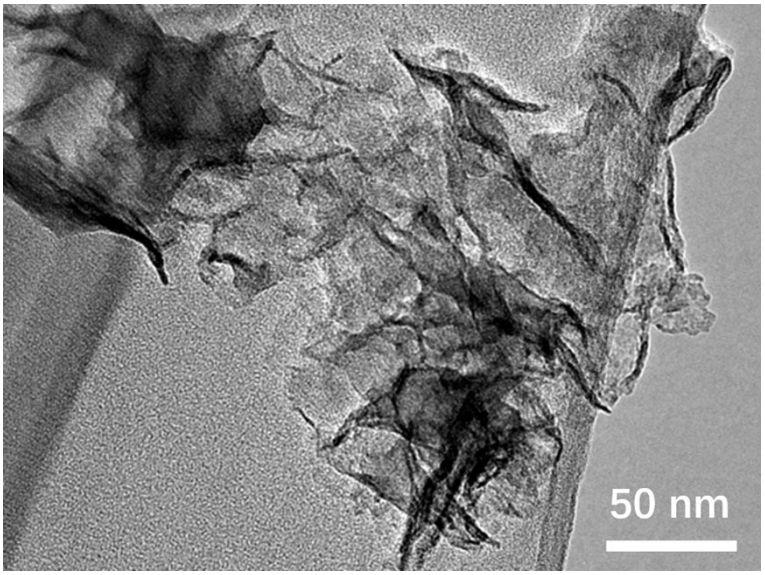

Fig. S5. FETEM image of the CoS_x NSs.

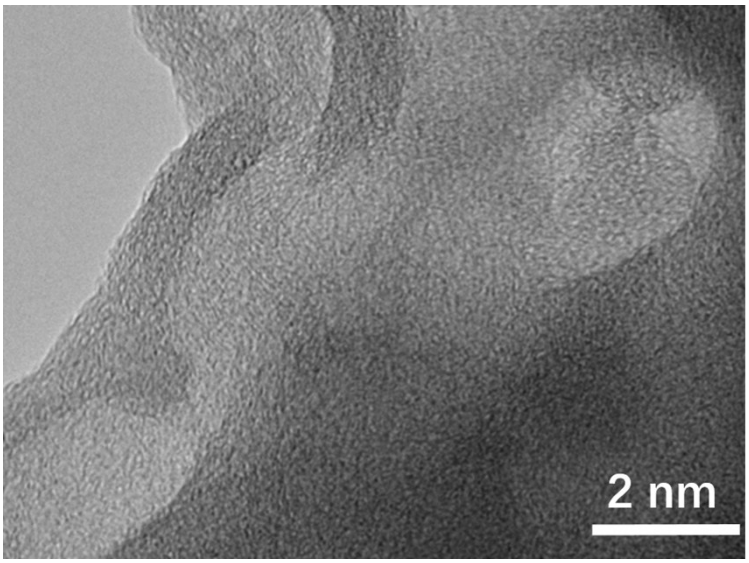

Fig. S6. HRTEM image of the CoS_x NSs.

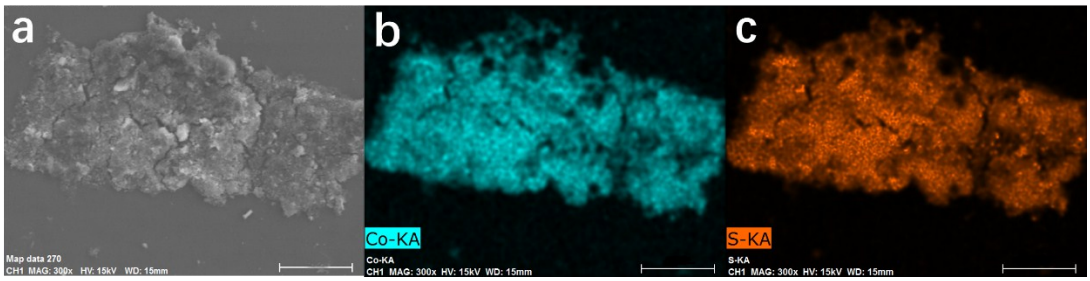

Fig. S7. SEM-EDX elemental mapping of the CoS_x NSs. a) SEM image. b) Co map. c) S map. Scale bars: 40 µm.

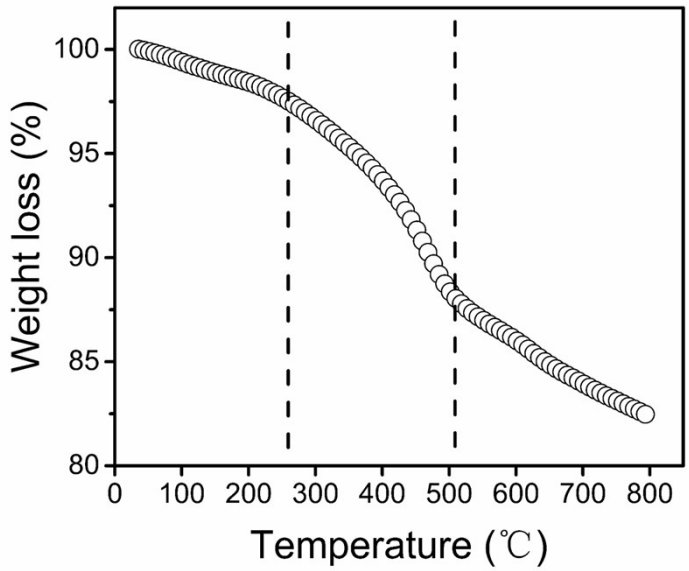

Fig. S8. TGA (temperature range: 25-800 °C heating rate at 5 °C min^{-1}) for as synthesized CoS_x NSs. This TGA have three distinct stage of weight losses, the first weight loss stage ended at 260 °C, stemming from evaporation of trace water with organic content, such as 1,2-ethanedithiol, n-butylamine and etc. The second weight loss stage was attributed to the de-sulfurization of CoS_x to form CoS phase, with a temperature range of 260-510 °C. This stage may include crystallization of the amorphous CoS_x, so the weight loss rate change slightly around 420 °C. Finally, the more stable of Co_9S_8 phase formed gradually.

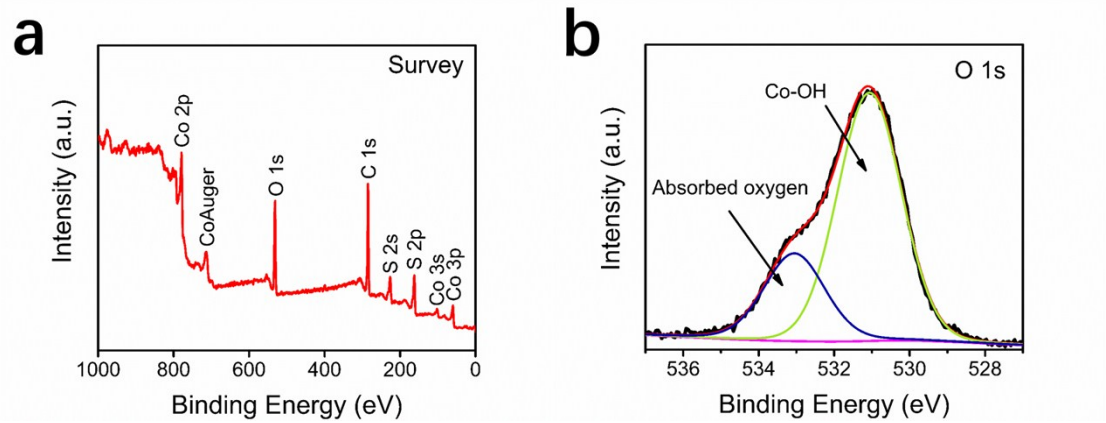

Fig. S9. XPS spectra of a) survey and b) O 1s of the CoS_x NSs.

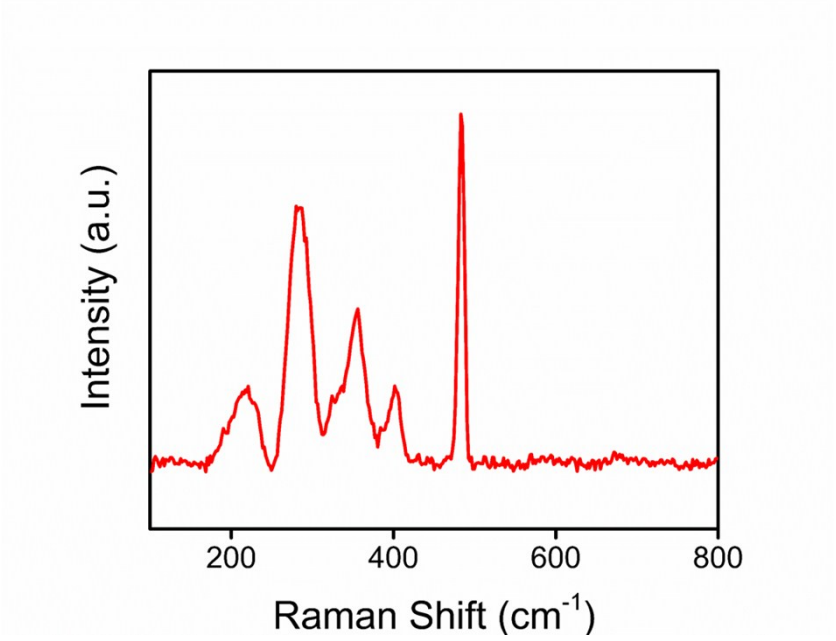

Fig. S10. A typical Raman spectrum of the CoS_x NSs.

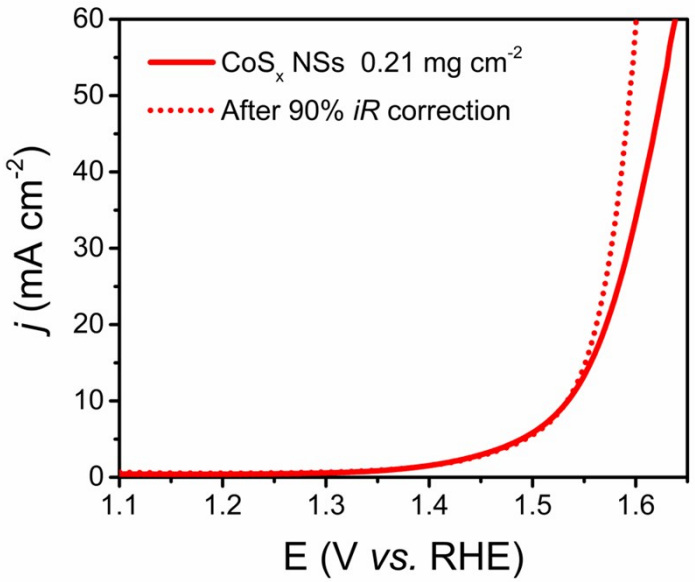

Fig. S11. Respective OER polarization curves of the CoS_x NSs in three-electrode configuration in 1.0 M KOH on GCE with identical loading mass, before and after 90% *iR* correction (*R* is series resistance). Scan rate: 5 mV s^{-1}. At small current density regions ($j \leq 12$ mA cm^{-2}), there is negligible difference in the values before and after *iR* correction.

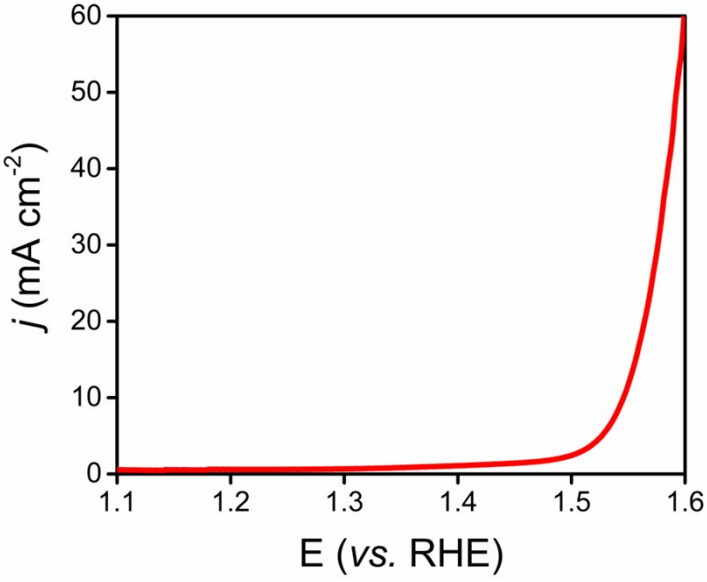

Fig. S12. LSV of the CoS_x NSs for OER in three-electrode configuration in 0.5 M H_2SO_4 loaded on GCE with a scan rate of 5 mV s^{-1}, with 90% *iR* correction.

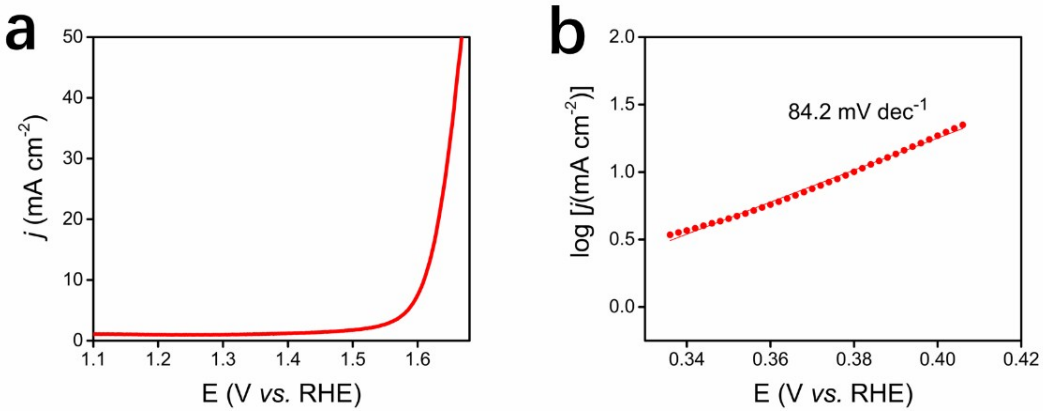

Fig. S13. a) LSV and b) Tafel slope of the CoS_x NSs for OER in three-electrode configuration in 1.0 M KOH loaded on Au (111) electrode with a scan rate of 5 mV s^{-1}, with 90% *iR* correction.

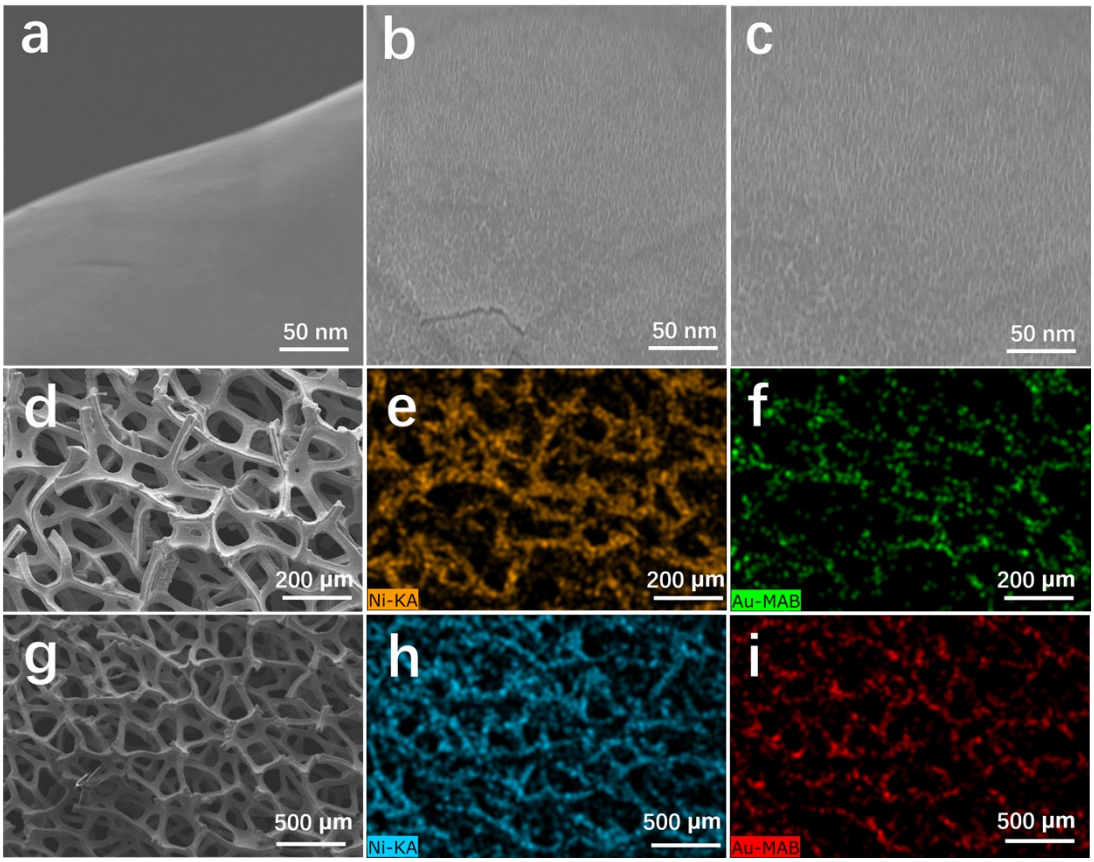

Fig. S14. FESEM images of a) bare nickel foam, b) nickel foam coated with gold by Magnetron sputtering (denote as gold-NF-1) and c) nickel foam coated with gold by electroplating (denote as gold-NF-2); d-f) SEM-EDX elemental mapping of gold-NF-1; g-i) SEM-EDX elemental mapping of gold-NF-2. The surface of bare nickel foam is smooth, while gold-NFs are both covered with uniform nanosheets, suggesting the successful coating with gold by the two methods. The element mapping also demonstrates the uniform gold coating on nickel foam.

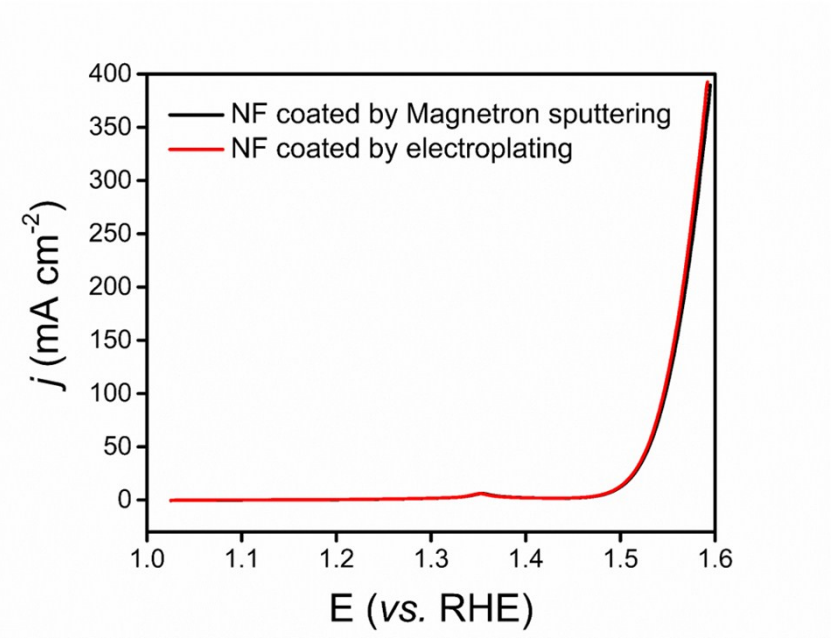

Fig. S15. LSV of the CoS_x NSs for OER in three-electrode configuration in 1.0 M KOH loaded on gold coated nickel foams with a scan rate of 5 mV s^{-1}, with 90% *iR* correction. There is no obvious difference on OER performance of the catalyst between Magnetron sputtering and electroplating methods.

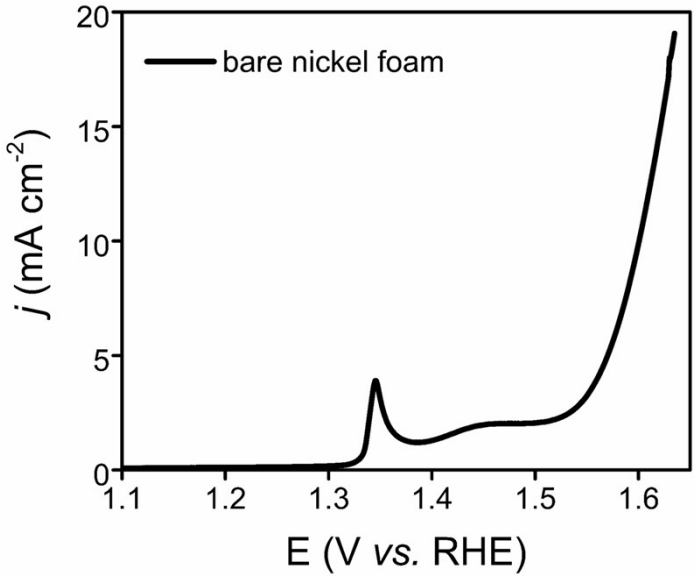

Fig. S16. LSV of bare nickel foam for OER in three-electrode configuration in 1.0 M KOH with a scan rate of 5 mV s^{-1}, with 90% *iR* correction. The small hump at ~1.35 V *vs.* RHE is anodic peak of nickel foam itself.

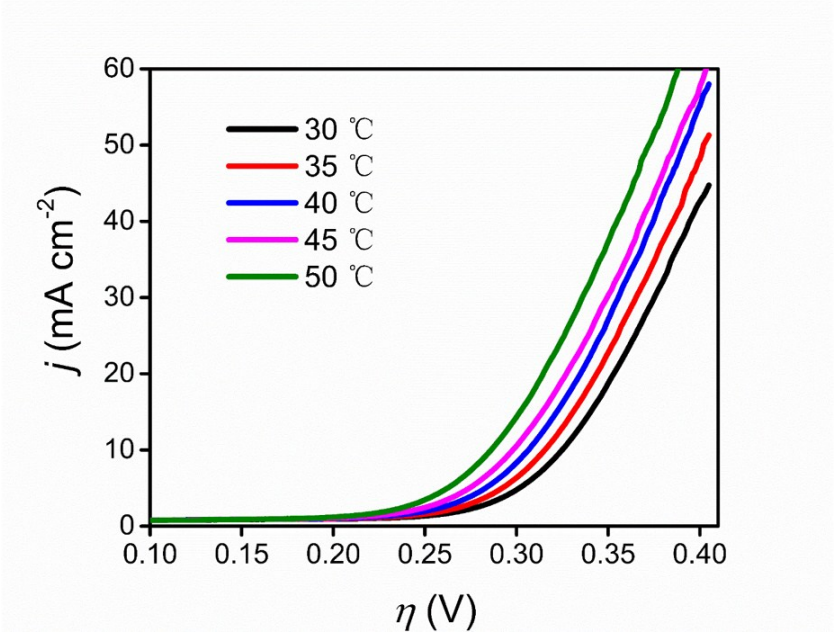

Fig. S17. LSV of the CoS_x NSs for OER in three-electrode configuration in 1.0 M KOH loaded on GCE with a scan rate of 5 mV s^{-1} at 30 °C, 35 °C, 40 °C, 45 °C and 50 °C, respectively, without *iR* correction.

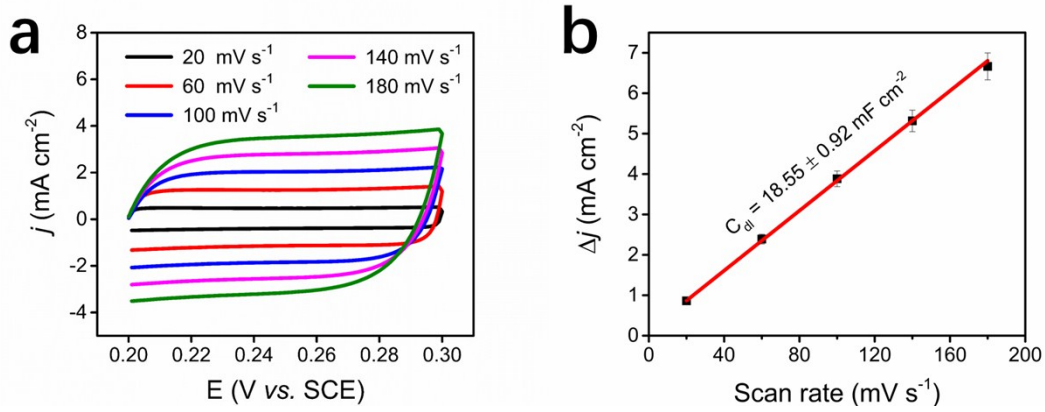

Fig. S18. a) CV and b) extraction of the C_{dl} of the CoS_x for OER in three-electrode configuration in 1.0 M KOH loaded on GCE with scan rates of 20 mV s^{-1}, 60 mV s^{-1}, 100 mV s^{-1}, 140 mV s^{-1} and 180 mV s^{-1}, respectively, without *iR* correction. ($\Delta j = j_a - j_c$).

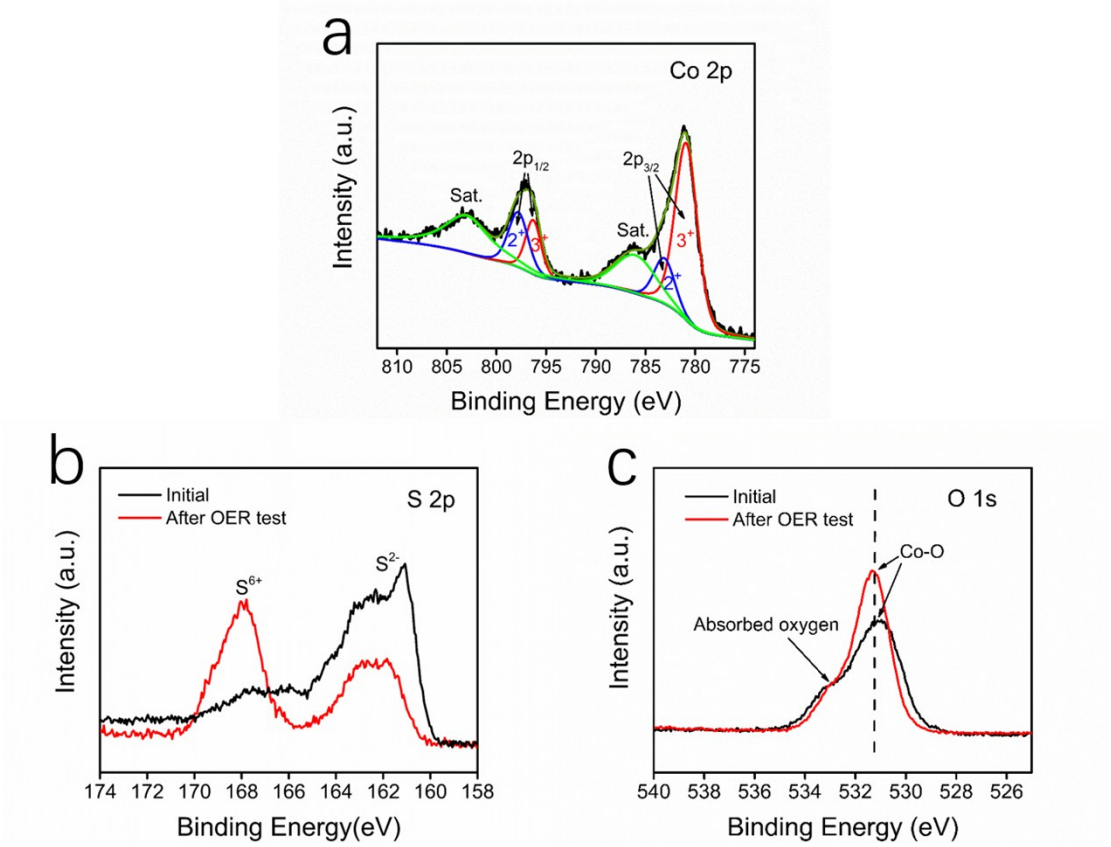

Fig. S19. XPS spectra a) Co 2p, b) S 2p and c) O 1s of CoS_x NSs after chrono-potentiometric experiment from Fig. 4d. In Co 2p spectrum, the increase of Co^{3+} (compared with Fig. 3a) after OER test might arise from the *in-situ* oxidation of Co^{2+} of Co-S in the CoS_x NSs.[7] Besides, the formation of Co-OOH[8] during OER test may also attribute to the increased Co^{3+} proportion. In S 2p spectrum, the decreased S^{2-} after OER test demonstrates the slight oxidation of CoS_x NSs. Also, the increased S^{6+} results from the further oxidation of S species.[9] In O 1s spectrum, the peaks at 531.2 eV and 533.0 eV are assigned to Co-O[8] of $CoOOH/Co(OH)_2$ and physisorption of oxygen or moisture[10] at/near the surface under ambient conditions, respectively. The intensity of Co-O/Co-OH increases after OER test while the peaks at 532 eV remain unchanged, suggesting the formation of $CoOOH/Co(OH)_2$. The formation of Co-O is due to the *in-situ* surface electrochemical oxidation of CoS_x during the OER process and the Co-O sites are electrochemically active for the OER process.[11] Therefore, we consider the interfaces between the in-situ formed Co-O and CoS_x are favourable for the OER process.[12]

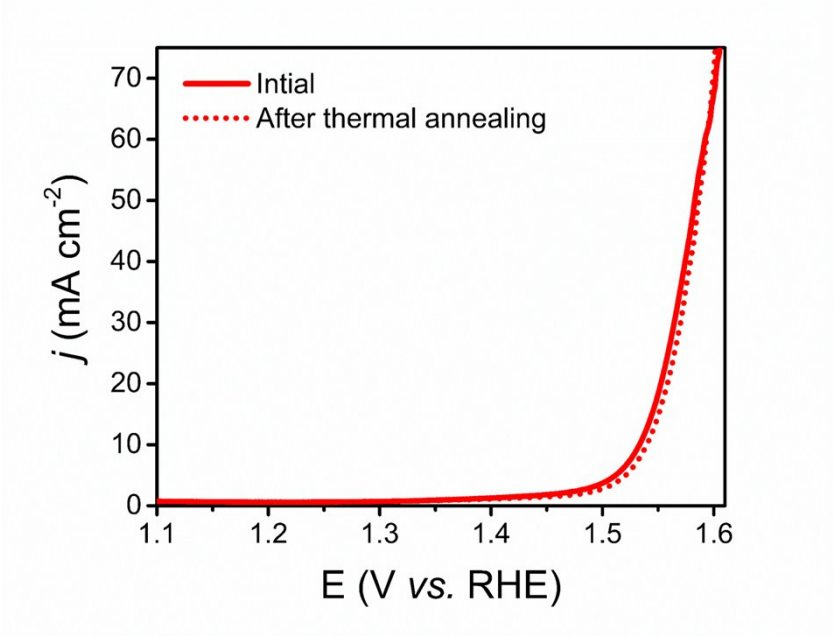

Fig. S20. OER performance of the CoS_x before and after 200 °C thermal annealing on GCE with scan rates of 5 mV s^{-1} in three-electrode configuration in 1.0 M KOH, with 90% *iR* correction. There is no obvious difference between the catalysts before and after 200 °C thermal annealing, demonstrating the high thermal stability of CoS_x NSs.

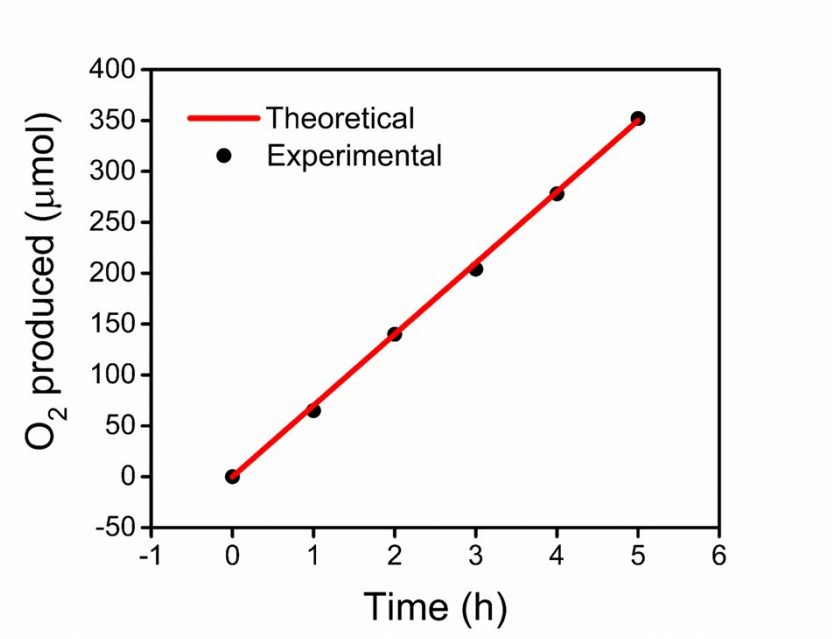

Fig. S21. Theoretical and experimental O_2 evolution amount of the CoS_x NSs loaded on gold-NF with a constant current of 7.5 mA.

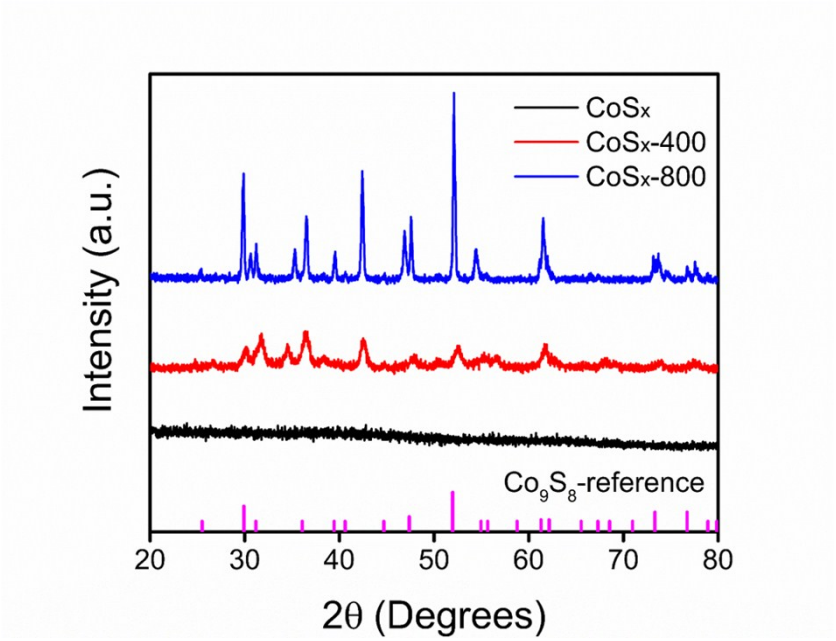

Fig. S22. The XRD patterns of CoS_x before and after annealing. The amorphous CoS_x transforms into relatively high-crystalline materials after annealing at 400 °C and 800 °C. The XRD pattern of CoS_x-400 and CoS_x-800 can be indexed to Co_9S_8 (JCPDS card no. 65-6801), which is consistent with the TGA consequence in Fig. S8.

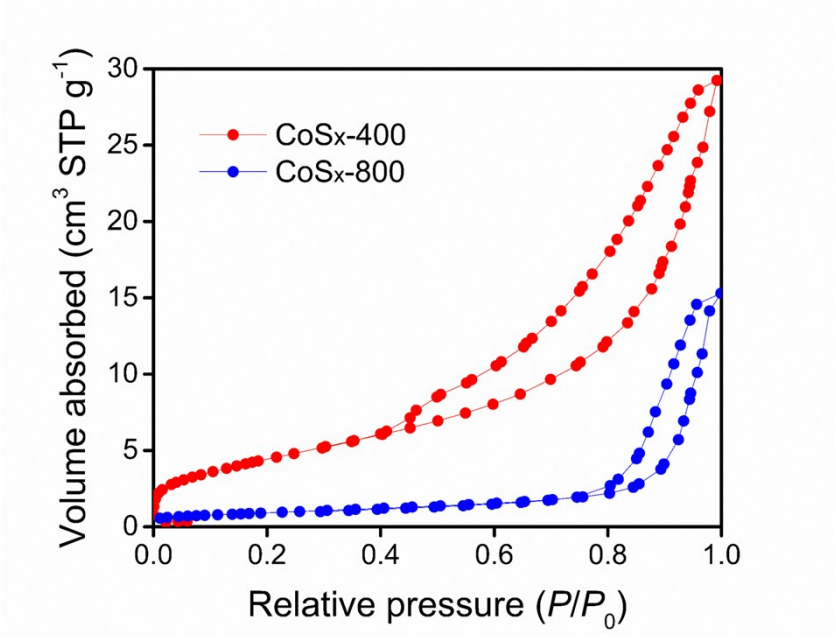

Fig. S23. N_2 adsorption and desorption isotherms for CoS_x-400 and CoS_x-800.

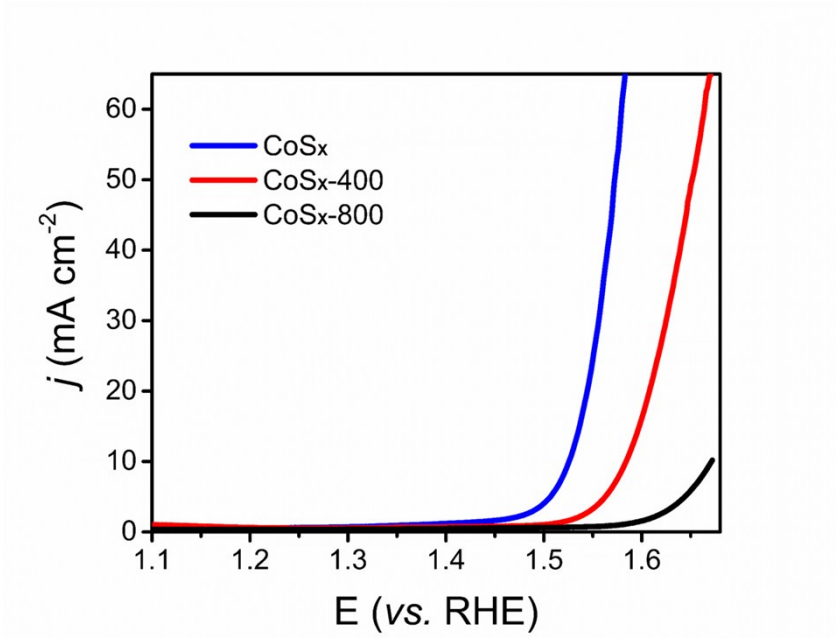

Fig. S24. LSV of CoS_x, CoS_x-400 and CoS_x-800 on GCE with a scan rates of 5 mV s^{-1} in three-electrode configuration in 1.0 M KOH, with 90% *iR* correction.

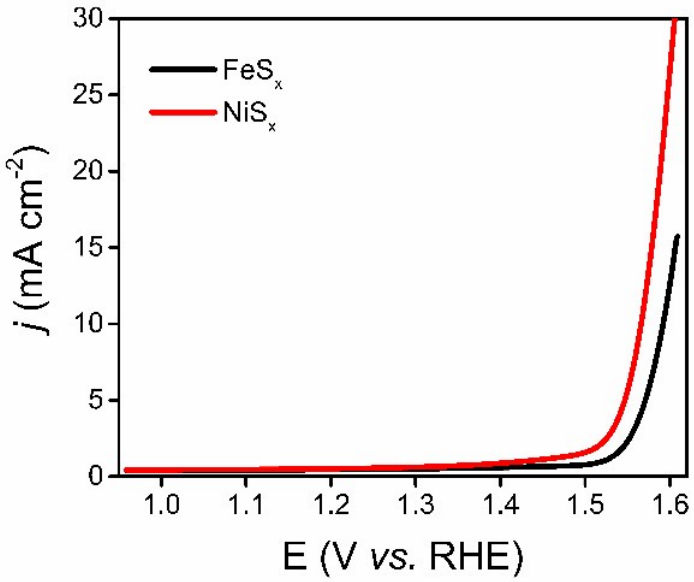

Fig. S25. OER performance of other catalysts obtained from EDT-BA quasi-ionic liquid in three-electrode configuration in 1.0 M KOH loaded on GCE with a scan rate of 5 mV s^{-1}, with 90% *iR* correction. The FeS_x and NiS_x catalysts were obtained from solutions of elemental iron and nickel(III) oxide, respectively.

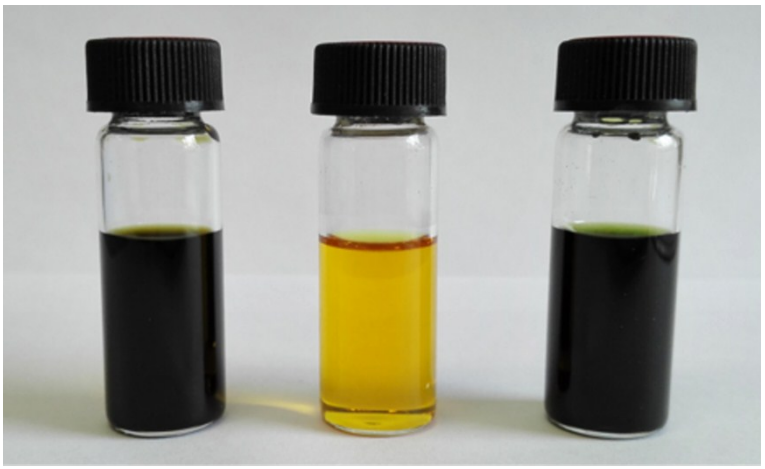

Co + S Se Co + S +Se

Fig. S26. The EDT-BA solutions of Co + S, Se and their mixes. After mixing with Se, the solution of Co-S turned to dark green, suggest the form of CoS_xSe_y.

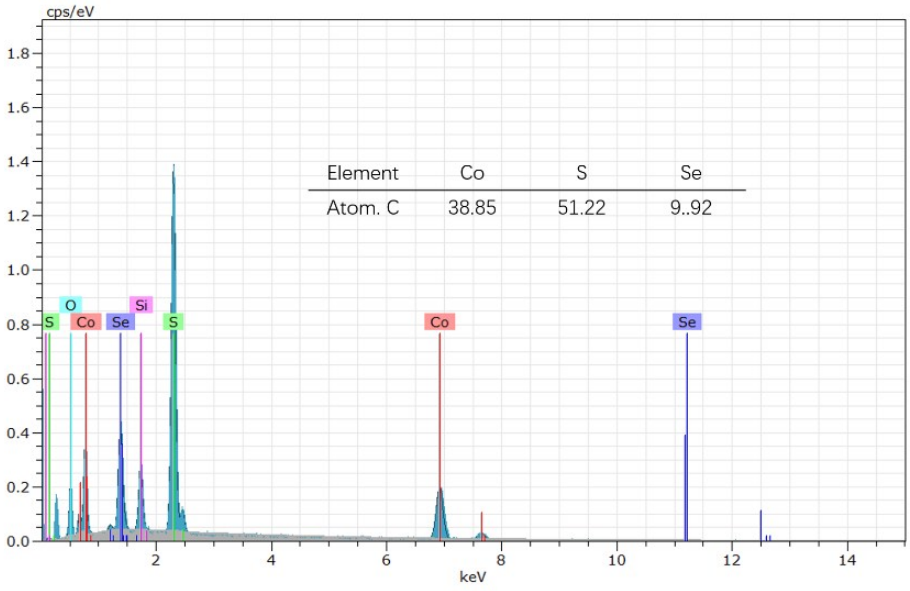

Fig. S27. EDX spectrum from SEM of the CoS_xSe_y. (Si and O peaks emanate from the SiO_2-coated Si wafer). Inset: the corresponding atomic ratio of CoS_xSe_y.

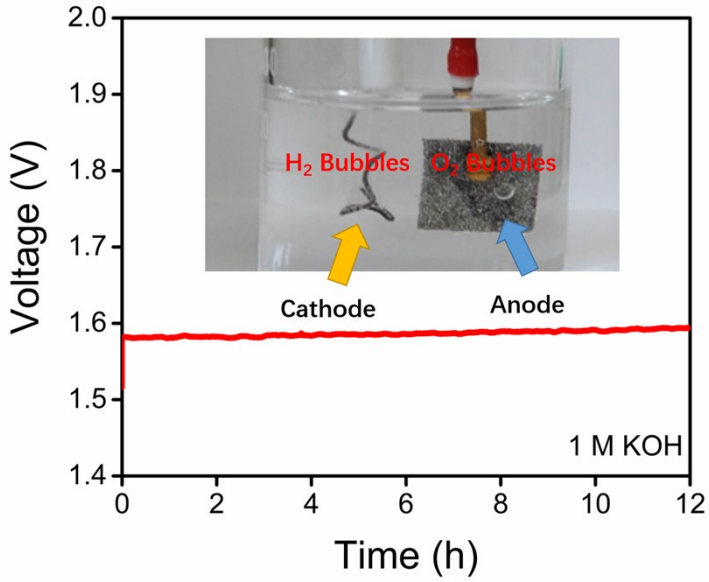

Fig. S28. Chrono potentiometric curve obtained with the Pt-CoS_x couple catalyst in two electrode setup in 1.0 M KOH solution. There is no appreciable increase in potential at the current density of 10 mA cm^{-2} over 12 h, confirming that the Pt- CoS_x couple catalyst is extremely stable in two electrode setup. The bubbles at both electrodes indicates a fast reaction. Current density of 10 mA cm^{-2} was delivered with a cell voltage of 1.58 V, that is, a combined overpotential of about 350 mV for electrochemical overall water splitting.

3. Supplementary Tables

Table S1. BET specific surface area of materials synthesized by different methods.

Catalyst	BET surface area (m^2g^{-1})	Synthetic method	Reference
CoS_x	24.2	Ambient synthesis	*This work*
Co_3S_4	12.26	Hydrothermal process	*13*
Co_9S_8@carbon	29	Thermal pyrolysis	*14*
Fe_3O_4@Co_9S_8/rGO	18	Solvothermal process	*15*
CoS_2/GO	19	Solid-state thermolysis	*16*
$(Co, Ni)_3S_2$	17.1	Hydrothermal process	*17*
Co_9S_8	16.9	Hydrothermal process	*18*

Table S2. The overpotential (j = 10 mA cm^{-2}) of IrO_2 in both acidic and alkaline mediums.

Catalyst [a]	Overpotential (mV)	Electrolyte	Reference
CoS_x	302	1.0 M KOH	*This work*
CoS_x	335	0.5 M H_2SO_4	*This work*
IrO_2	340	1.0 M KOH	*19*
IrO_2	470	0.1 M KOH	*20*
IrO_2	330	0.5 M H_2SO_4	*21*
IrO_2	420	0.1 M $HClO_4$	*20*
IrO_2	324	0.1 M $HClO_4$	*22*
IrO_2	310	0.5 M H_2SO_4	*23*
IrO_2	389	0.1 M $HClO_4$	*24*

[a] The catalyst is loaded on GCE.

Table S3. Co-based catalysts for OER in 1.0 M KOH in recent publications.

Catalyst	Substrate	Overpotential at 10 mA cm^{-2} (mV)	Tafel slope (mV dec^{-1})	Reference
CoS_X	GCE	302	64.8	*This work*
CoS_X	Ni foam	271	48.8	*This work*
Co-S/CTs	Carbon paper	306	72	*25*
Co_3O_4/MNTs	Ni foam	353	80	*26*
CoS_2/N,S-GO	GCE	380	75	*16*
Co_4N/CNW	Caron cloth	310	81	*27*
Co_9S_8@NOSC	GCE	340	68	*14*
Co-P films	Cu foil	345	47	*28*
Co_9S_8@MoS_2/CNF	GCE	430	61	*29*
CoP	Au foil	300	65	*30*
$Co_{0.85}Se$	Carbon cloth	324	85	*31*
Fe_3O_4@Co_9S_8/rGO	GCE	340	54.5	*15*
$CoS_{4.6}O_{0.6}$	GCE	290	67	*32*

4. Supplementary References

1 D. H. Webber and R. L. Brutchey, *J. Am. Chem. Soc.*, 2013, **135**, 15722-15725.

2 X. Sun, Z. Xue and T. Mu, *Green Chem.*, 2014, **16**, 2102-2106.

3 D. Stueber, D. Patterson and R. W. Parry, *Inorg. Chem.*, 2001, **40**, 1902-1911.

4 J. Elias, M. Gizowska, P. Brodard, R. Widmer, Y. Dehazan, T. Graule, J. Michler and L. Philippe, *Nanotechnology*, 2012, **23**, 255705.

5 J. R. Swierk, S. Klaus, L. Trotochaud, A. T. Bell and T. D. Tilley, *J. Phys. Chem. C*, 2015, **119**, 19022-19029.

6 J. Yin, Q. Fan, Y. Li, F. Cheng, P. Zhou, P. Xi and S. Sun, *J. Am. Chem. Soc.*, 2016, **138**, 14546-14549.

7 M. K. Halbert and R. P. Baldwin, *Anal. Chem.*, 1985, **57**, 591–595.

8 J. Yang, H. Liu, W. N. Martens and R. L. Frost, *J. Phys. Chem. C*, 2010, **114**, 111-119.

9 M. Al-Mamun, Y. Wang, H. Yang, D. Wang, Z. Tang and H. Zhao, *J. Mater. Chem. A*, 2016, **4**, 18314-18321.

10 Y. Wang, J. Tang, B. Kong, D. Jia, Y. Wang, T. An, L. Zhang and G. Zheng, *RSC Adv.*, 2015, **5**, 6886-6891.

11 M. Favaro, J. Yang, S. Nappini, E. Magnano, F. M. Toma, E. J. Crumlin, J. Yano and I. D. Sharp, *J. Am. Chem. Soc.*, 2017, **139**, 8960-8970.

12. J. Zhang, T. Wang, D. Pohl, B. Rellinghaus, R. Dong, S. Liu, X. Zhuang and X. Feng, *Angew. Chem. Int. Ed.*, 2016, **55**, 6702–6707.

13 P. Sennu, M. Christy, V. Aravindan, Y.-G. Lee, K. S. Nahm and Y.-S. Lee, *Chem. Mater.*, 2015, **27**, 5726-5735.

14 S. Huang, Y. Meng, S. He, A. Goswami, Q. Wu, J. Li, S. Tong, T. Asefa and M. Wu, *Adv. Funct. Mater.*, 2017, **27**, 1606585.

15 J. Yang, G. Zhu, Y. Liu, J. Xia, Z. Ji, X. Shen and S. Wu, *Adv. Funct. Mater.*, 2016, **26**, 4712-4721.

16 P. Ganesan, M. Prabu, J. Sanetuntikul and S. Shanmugam, *ACS Catal.*, 2015, **5**, 3625-3637.

17 Z. Li, X. Li, L. Xiang, X. Xie, X. Li, D.-R. Xiao, J. Shen, W. Lu, L. Lu and S. Liu, *J. Mater. Chem. A*, 2016, **4**, 18335-18341.

18 J. Huo, J. Wu, M. Zheng, Y. Tu and Z. Lan, *J. Power Sources*, 2016, **304**, 266-272.

19 F. Song and X. Hu, *J. Am. Chem. Soc.*, 2014, **136**, 16481-16484.

20 Y. Lee, J. Suntivich, K. J. May, E. E. Perry and Y. Shao-Horn, *J Phys. Chem. Lett.*, 2012, **3**, 399-404.

21 P. P. Patel, M. K. Datta, O. I. Velikokhatnyi, R. Kuruba, K. Damodaran, P. Jampani, B. Gattu, P. M. Shanthi, S. S. Damle and P. N. Kumta, *Sci. Rep.*, 2016, **6**, 28367.

22 I. Spanos, A. A. Auer, S. Neugebauer, X. Deng, H. Tüysüz and R. Schlögl, *ACS Catal.*, 2017, **7**, 3768-3778.

23 C. Massué, X. Huang, A. Tarasov, C. Ranjan, S. Cap and R. Schlögl, *ChemSusChem*, 2017, **10**, 1958.

24 W. Sun, Y. Song, X.-Q. Gong, L.-m. Cao and J. Yang, *Chem. Sci.*, 2015, **6**, 4993-4999.

25 J. Wang, H. X. Zhong, Z. L. Wang, F. L. Meng and X. B. Zhang, *ACS Nano*, 2016, **10**, 2342-2348.

26 H. Wang, S. Zhuo, Y. Liang, X. Han and B. Zhang, *Angew. Chem. Int. Ed.*, 2016, **55**, 9055-9059.
27 F. Meng, H. Zhong, D. Bao, J. Yan and X. Zhang, *J. Am. Chem. Soc.*, 2016, **138**, 10226-10231.
28 N. Jiang, B. You, M. Sheng and Y. Sun, *Angew. Chem. Int. Ed.*, 2015, **54**, 6251-6254.
29 H. Zhu, J. Zhang, R. Yanzhang, M. Du, Q. Wang, G. Gao, J. Wu, G. Wu, M. Zhang, B. Liu, J. Yao and X. Zhang, *Adv. Mater.*, 2015, **27**, 4752-4759.
30 Y. Yang, H. Fei, G. Ruan and J. M. Tour, *Adv. Mater.*, 2015, **27**, 3175-3180.
31 C. Xia, Q. Jiang, C. Zhao, M. N. Hedhili and H. N. Alshareef, *Adv. Mater.*, 2016, **28**, 77-85.
32 L. Zhuang, L. Ge, Y. Yang, M. Li, Y. Jia, X. Yao and Z. Zhu, *Adv. Mater.*, 2017, **29**, 1606793.